DOI: 10.1002/ejic.200501021

A New $Bi_4Mn_{1/3}W_{2/3}O_8Cl$ Sillén–Aurivillius Intergrowth: Synthesis and Structural Characterisation by Quantitative Transmission Electron Microscopy

David Ávila-Brande,*[a] L. Carlos Otero-Díaz,[a,b] Ángel R. Landa-Cánovas,[c] Sara Bals,[d] and Gustaaf Van Tendeloo[d]

Keywords: Sillén–Aurivillius intergrowths / Layered oxyhalide / Electron microscopy / Exit-wave reconstruction / Bismuth

The synthesis and structural characterisation of a new phase with nominal composition $Bi_4Mn_{1/3}W_{2/3}O_8Cl$ is presented. Conventional and analytical transmission electron microscopy are used to determine the composition, unit-cell symmetry and space group of the compound, whereas a structural model is deducted by exit-wave reconstruction in the transmission electron microscope. This technique allows the microscope information limit of 1.1 Å to be reached and the (light) oxygen atoms in the presence of heavier atoms (Bi, W, Mn) to be imaged. The average structure is refined from X-ray powder diffraction data using the Rietveld method yielding an orthorhombic unit cell with lattice parameters a = 5.467(4) Å, b = 5.466(7) Å and c = 14.159(3) Å and space group $Cm2m$, which could be described as a Sillén–Aurivillius intergrowth.

Introduction

Bismuth-based systems have been extensively studied because of their ability to form new complex intergrowth structures with variable properties. For example, the high Tc superconducting bismuth phases[1,2] can be described as an alternation of n slabs of perovskite-like layers with a double $[BiO]^+$ layer. Related to those structures, the Aurivillius phases with general composition $[Bi_2O_2][A_{n-1}B_nO_{3n+1}]$ are built up as a regular intergrowth of perovskite slabs $[A_{n-1}B_nO_{3n+1}]^{2-}$ and $[Bi_2O_2]^{2+}$ fluorite layers.[3,4] Despite the structural similarities, superconducting properties have not yet been found for the Aurivillius phases, whereas ferroelectric properties with large spontaneous polarisations[5] and high Curie temperatures[6] have been reported.

The complex oxyhalides described by Sillén[7] form another structural variant of layered compounds containing the $[Bi_2O_2]^{2+}$ structural block. These compounds are built up from single, double or triple halide ion sheets separated by $[Bi_2O_2]^{2+}$ layers.

The presence of the $[Bi_2O_2]^{2+}$ layer in the Aurivillius phases as well as in the Sillén complex oxyhalides suggests that intergrowth in these structures might yield a number of new phases. In fact, Aurivillius reported a number of intergrowths with the general sequence $[Bi_2O_2][A_{n-1}B_nO_{3n+1}]$-$[Bi_2O_2][X_m]$ in which A is a large cation (A: Bi^{3+}, Pb^{2+}, Sr^{2+}), B a small transition metal (B: Nb^{5+}, Ta^{5+}, W^{6+}, Ti^{4+}, Al^{3+}) and X a halide (Cl, Br).[8] In the above sequence, n denotes the thickness of the perovskite layers in terms of $\{BO_6\}$ octahedra and m the number of halide slabs.

The general formula for the simplest member (n = 1 and m = 1) of the Sillén–Aurivillius intergrowth can be written as Bi_4BO_8X and hence B must be a pentavalent cation. However, if another lone pair cation like Pb^{2+} with a lower oxidation state substituting for Bi^{3+} is introduced, the B cation must be replaced by a hexavalent one like W^{6+}.

Aurivillius[8] was the first to synthesise the Bi_4NbO_8Cl and $PbBi_3WO_8Cl$ phases. His characterisation indicated a phase mixture (c_1 = 14.5 Å and c_2 = 29.0 Å) for Bi_4NbO_8Cl and a single phase for $PbBi_3WO_8Cl$ ($a \approx b$ = 5.51 Å; c = 14.35 Å; space group $Cm2m$). Ackerman[9] revised these structures and assigned the orthorhombic space group $P2_1cn$ to the niobium oxychloride Bi_4NbO_8Cl ($a \approx b$ = 5.49 Å and c = 28.75 Å) and the tetragonal space group P_4 ($a = b$ = 3.84 Å; c = 14.35 Å) to $PbBi_3WO_8Cl$. Recently, Kusainova et al.[10] reanalysed the structure of Bi_4NbO_8Cl by using neutron diffraction powder data in the same $P2_1cn$ space group (a = 5.44 Å, b = 5.49 Å and c = 28.81 Å). A study of the ferroelectric properties yields a T_c of 765 K.

By inserting adequate transition metals in the Aurivillius block, phases with interesting electric and magnetic properties can be obtained. Manganese, for example, has attracted great attention because of the colossal magnetoresistance (CMR) observed in manganese perovskites.[11,12] In this work, we present the synthesis as well as the structural char-

[a] Dpto. Química Inorgánica, Fac. CC. Químicas, Universidad Complutense,
28040 Madrid, Spain
E-mail: david@brunilda.sme.ucm.es
[b] Centro de Microscopía, Universidad Complutense,
28040 Madrid, Spain
[c] Inst. Ciencia de Materiales de Madrid, CSIC,
28049 Madrid, Spain
[d] Electron Microscopy for Materials Science (EMAT), University of Antwerp,
Groenenborgerlaan 171, 2020 Antwerpen, Belgium

acterisation of a new phase with nominal composition $Bi_4Mn_{1/3}W_{2/3}O_8Cl$.

Results and Discussion

Composition Analysis and Mn Oxidation State Determination

X-ray energy dispersive spectroscopy (XEDS) analyses performed on several microcrystallites yield an average composition $Bi_{3.99(2)}Mn_{0.33(1)}W_{0.70(7)}Cl_{0.62(9)}$. The measured chlorine content is lower than the nominal value, which is due to severe overlapping between the Bi–M_α and the Cl–K_α peak, making it impossible to assert the presence of chlorine using XEDS. The chlorine edge is more distinctly present in the electron energy loss spectrum (EELS) presented in Figure 1, which shows the chlorine-$L_{2,3}$ absorption edge at 200 eV and the oxygen-K edge at 532 eV. The carbon-K edge at 284 eV is due to the carbon coating grid of the transmission electron microscopy (TEM) specimen-supporting grid.

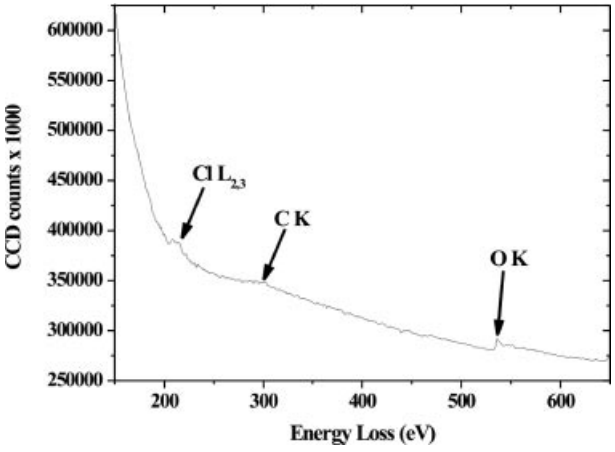

Figure 1. EEL spectrum showing the presence of the different lighter elements (Cl, O).

Figure 2 shows the magnetic susceptibility curve, with the χ^{-1} curve shown as an inset. This curve obeys the Curie–Weiss law between 50 and 300 K and μ_{eff} equals $5.20\mu_B$.

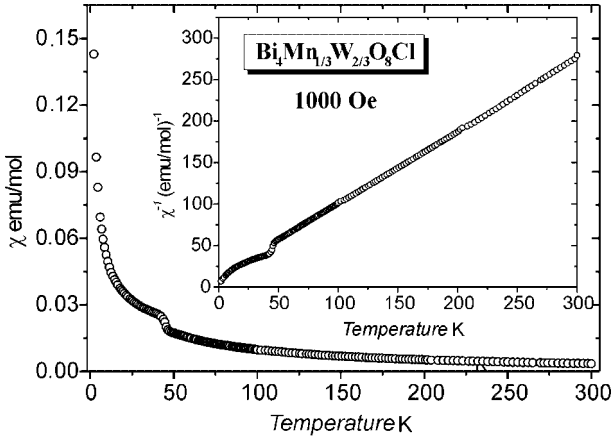

Figure 2. Curve of the magnetic susceptibility vs. temperature. The inset shows the χ^{-1} curve for the sample.

This value is slightly higher than the theoretical one ($4.90\mu_B$)[13] corresponding to a high-spin Mn^{3+}.

Unit Cell and Symmetry Determination

Selected area electron diffraction (SAED) patterns of several crystals show a homogeneous sample with an either tetragonal primitive cell ($a_o = b_o = 3.8$ Å and $c_o = 14.1$ Å) or a pseudotetragonal centred one ($a \approx b = 2a_o = 5.4$ Å and $c = 14.1$ Å). In order to distinguish between the two, microdiffraction is performed following the method proposed by Morniroli and Steeds.[14] It is important to note that in Mornirolli's work, the lattice parameters for the orthorhombic system were chosen such that $c < a < b$, whereas we have chosen the setting *bca* taking into account the variation in the zone axes notation, for example, [001] changes to [010] after the application of the *bca* setting.

In the first step the crystal system is determined. The experimental [010] pattern, which displays the highest "net" symmetry, has (2mm) symmetry for the zero-order Laue zone (ZOLZ) and 2mm for the whole pattern [ZOLZ + first-order Laue zone (FOLZ)] (Figure 3, a). According to Table 7 in ref.[14] the crystal system is therefore orthorhombic. In order to determine the Bravais lattice as well as the presence of glide planes, a comparison between experimental and simulated [001] and [010] microdiffraction patterns is made (Figure 3, parts a and b). The [001] zone axis contains a "net" mirror m1 in the ZOLZ and the FOLZ reflections; the [010] pattern on the other hand exhibits two perpendicular "net" mirrors m1 and m2 in both the ZOLZ and FOLZ, but the shift between the ZOLZ and the FOLZ reflections parallel to the m2 allows identification of a C centring. According to ref.[15] this gives the extinction symbols:

C.-. for [010]

C..- for [001]

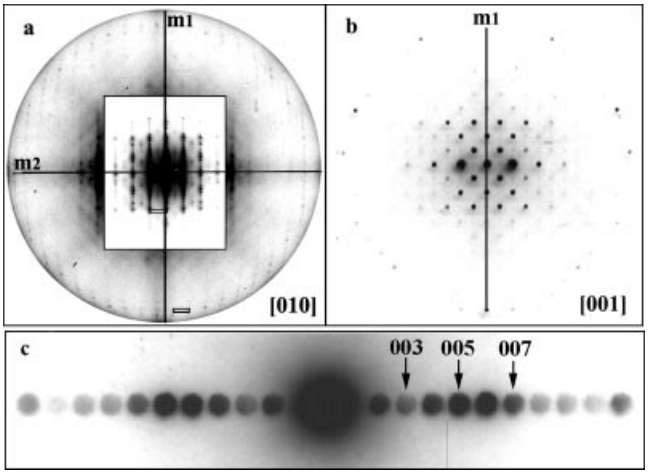

Figure 3. Microdiffraction patterns along (a) [010] and (b) [001]. (c) Enlarged systematic row from [010] showing the 00*l* reflections.

Combining these results, we find a partial extinction symbol C.-- (Table 1), which is in agreement with two pos-

sible space groups: *Cm*2*m* and *Cc*2*m*.[15] When looking at the magnified central row of the [010] zone (Figure 3, c) it is easy to note the presence of 00*l* reflections with $l = 2n + 1$. The absence of Gjønnes–Moodie lines in those reflections indicates that they are kinematically allowed. The distinction between both can be made by analysing the reflections listed in Table 2. In *Cc*2*m* the 00*l* reflections with $l = 2n + 1$ are forbidden, whereas they are allowed in *Cm*2*m*. Figure 4 shows that 00*l* reflections with $l = 2n + 1$ are observed along the [010] and [1–10] zone axes. *Cm*2*m* is therefore identified as the correct space group for $Bi_4Mn_{1/3}W_{2/3}O_8Cl$, which is isostructural with $Bi_4Ti_{1/2}W_{1/2}O_8Cl$[16] and lattice parameters $a \approx b = 5.4$ Å and $c = 14.1$ Å.

Table 1. "Net" and "ideal" symmetries as well as the extinction symbols.

$Bi_4Mn_{1/3}W_{2/3}O_8Cl$	Symmetries (N = "net"; I = "ideal")			
	b = [010]		*c* = [001]	
	N	I	N	I
ZOLZ	(2mm)	(2mm)	(m)	(m)
FOLZ	2mm	2mm	m	m
Extinction symbol	C.-.		C..-	

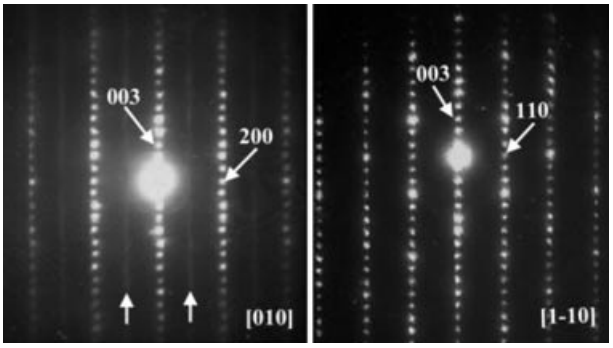

Figure 4. SAED patterns of $Bi_4Mn_{1/3}W_{2/3}O_8Cl$ along the [010] and [1–10] zone axes.

SAED patterns along the main zone axes reveal a well-ordered phase. Only the presence of a weak streaking along [10*l*] in the [010] zone axis (Figure 4, indicated by arrows) indicates some defects or extra ordering.

Structure Model Determination by Exit-Wave Reconstruction

Although high-resolution electron microscopy (HREM) is considered as a standard technique to image the atomic structure of materials, interpretation is not always straightforward because of aberrations of the electromagnetic lens system. The information that can be obtained by qualitative HREM is therefore limited by the Scherzer point-resolution, but for a coherent electron source (field emission gun) the information limit of the microscope reaches beyond this point-resolution. The information limit can be reached by correcting the phase changes due to the spherical aberration (C_s) of the objective lens. Exit-wave reconstruction uses a set of images taken from the same area but for different defocus values of the objective lens. The idea is to invert the image formation process so that lens aberrations can be eliminated and a better resolution can be obtained. A great advantage of this inversion is that the amplitude as well as the phase of the exit wave (i.e., the electron wave leaving the specimen) is reconstructed. As the light atom columns are revealed in the phase of the exit wave,[17] we are able to image the light oxygen atoms in the presence of heavy Bi, W and Mn atoms. In this manner, we directly obtain the projected coordinates, which allow us to build a structural model, assuming the *Cm*2*m* space group.

A focal series of 20 images with an equidistant focal decrease is recorded along the [1–10] zone axis using a slow-scan CCD camera. After reconstruction, using the TrueImage software, and correction for the aberrations, the complex exit wave is retrieved and split into amplitude and phase.

Figure 5 shows the phase of the reconstructed exit wave with the atom positions corresponding to the bright dots; the projected unit cell is outlined. The projected coordinates are directly determined from the phase image and the results are listed together with the ideal positions deduced for the *Cm*2*m* space group in Table 3.

The phase image clearly shows the projected octahedra $\{WO_6\}/\{MnO_6\}$ and it should be noted that also the oxygen atoms are revealed; they are indicated in Figure 5. We have fixed the W/Mn position in the origin (0,0,0) corresponding to the Wyckoff site *2a*. If we assume a model based on a Sillén–Aurivillius intergrowth, the octahedral layer from the Aurivillius block presents eight oxygens in two nonequivalent positions: four in the apex [called O(1)] and four in the equatorial plane [called O(2)]. From the reconstructed phase we can easily determine the projected positions for both, which correspond to 4c and 4d positions respectively in an ideal model.

Two types of bismuth, that is, Bi(1) and Bi(2), are present. Next to Bi(2) we can still observe smaller dots corresponding to the O(3) oxygen. Around Bi(1) we can also observe an extension of the blobs corresponding to the O(3)

Table 2. Reflection conditions for the two possible space groups.

Space group	Reflection conditions						
	hkl	**0*kl***	*h*0*l*	*hk*0	*h*00	0*k*0	**00*l***
*Cm*2*m*	$h + k = 2n$	$\mathbf{k = 2n}$	$h = 2n$	$h + k = 2n$	$h = 2n$	$k = 2n$	–
*Cc*2*m*	$h + k = 2n$	$\mathbf{k,l = 2n}$	$h = 2n$	$h + k = 2n$	$h = 2n$	$k = 2n$	$\mathbf{l = 2n}$

Table 3. Measured and determined coordinates from the ESW-phase image along [1–10].

Atom	Coordinates measured in the phase image		Site	Coordinates determined in the space group *Cm*2*m*		
	$\sqrt{(x^2 + y^2)}$	*z*		*x*	*y*	*z*
Bi(1)	0	0.35	*4c*	0	0	0.35
Bi(2)	0.5	0.18	*4c*	0	0.5	0.18
W	0	0	*2a*	0	0	0
Mn	0	0	*2a*	0	0	0
Cl	0.5	0.5	*2b*	0	0.5	0.5
O(1)	0	0.12	*4c*	0	0	0.12
O(2)	0.31	0	*4d*	0.22	0.22	0
O(3)	0.31	0.31	*8f*	0.22	0.22	0.31

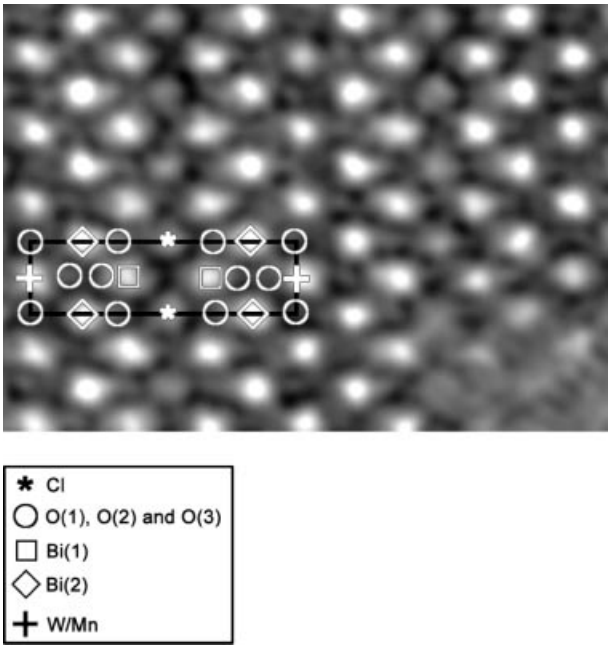

Figure 5. Phase of the reconstructed exit wave along [1–10]. The bright dots correspond to the projected position of the different atoms.

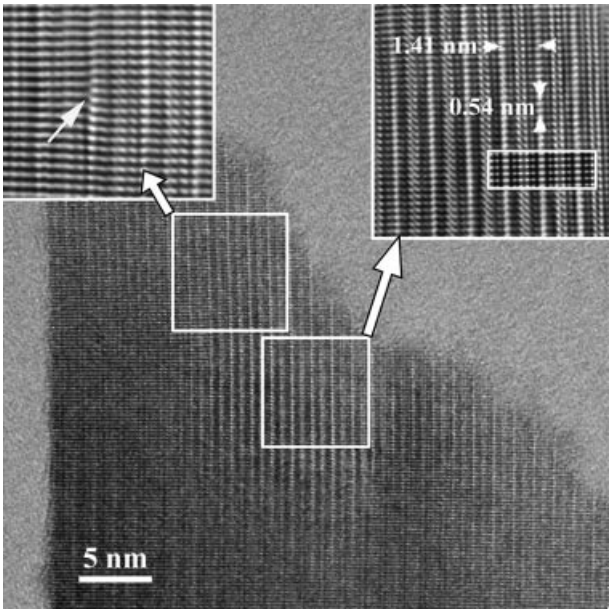

Figure 6. Experimental [010] HREM image. The upper-right enlarged area is a filtered image and shows a good match between the experimental and the simulated image (Δf = –300 Å; t = 30 Å). The filtered image on the left shows the presence of a dislocation marked by an arrow.

atoms. As the projected distance Bi(1)–O(3) is equal to 0.97 Å, which is below the information limit, it is not possible to observe Bi(1) and O(3) separately.

The measured coordinate for O(3) is only in agreement with the site symmetry *8f* for the *Cm*2*m* space group. Finally, the chlorine atom was located in a *2b* site according to the coordinates determined in the image. A more accurate fit of the projected positions of the atomic columns is being performed using statistical parameter estimation.[18]

Figure 6 displays an HREM image recorded along the [010] zone, with an enlarged (filtered) area presented as an inset on the right. This inset also shows a simulated part, which was calculated starting from the structural model obtained by exit-wave reconstruction (defocus value Δf = –300 Å, sample thickness was 30 Å). Obviously, a good fit between the experimental image and the simulated one is found. Here, the cation positions correspond to the dark dots. The only defects observed in the HREM images are dislocations; one of them is marked with an arrow in the filtered image shown as an inset on the left.

Average Structure: Powder X-ray Diffraction Refinement

Once the unit cell, the space group and the structural model are determined from electron microscopy data, the refinement of the average structure is carried out by X-ray powder diffraction.

The Rietveld refinement of $Bi_4Mn_{1/3}W_{2/3}O_8Cl$ (Figure 7) is performed using the structural data obtained from the phase of the reconstructed exit wave (see Table 3). Because of the stronger X-ray scattering of Bi^{3+}, Mn^{3+} and W^{6+}, the isotropic atomic displacement parameters (ADPs) of chlorine and oxygen atoms are all fixed at a reasonable value of 0.8 Å^2. Table 4 summarises the refined structural parameters; the R factors of weighted pattern (R_{wp}), pattern (R_p) and Bragg (R_B) converge to 16.1%, 12.9% and 5.87% respectively. These values agree with those obtained in other Aurivillius[19,20] and Sillén–Aurivillius[8] phases. It is worth mentioning that the high B value obtained for Bi(2) in the refinement agrees with our previous work on the isostructural $Bi_4Ti_{1/2}W_{1/2}O_8Cl$ compound.[16] This high value

Table 4. Refined structural parameters and main interatomic distances for $Bi_4Mn_{1/3}W_{2/3}O_8Cl$ phase.

Atom	Site	*x*	*y*	*z*	*B* [Å^2]	*n*	Distances [Å]		
Bi(1)	*4c*	0	0.004(8)	0.364(5)	0.33(6)	0.5	Bi(1)–O(3)	2.14(7)	x2
Bi(2)	*4c*	0	0.528(8)	0.181(2)	1.6(1)	0.5	Bi(1)–O(3)	2.17(7)	x2
W	*2a*	0	0.013(1)	0	0.3(1)	0.1666	Bi(1)–Cl	3.26(6)	x1
Mn	*2a*	0	0.013(1)	0	0.3(1)	0.0833	Bi(1)–Cl	3.34(1)	x2
Cl	*2b*	0	0.521(7)	0.5	0.8	0.25	Bi(1)–Cl	3.41(3)	x1
O(1)	*4c*	0	–0.083(7)	0.117(1)	0.8	0.5	Bi(2)–O(3)	2.51(6)	x2
O(2)	*4d*	0.188(1)	0.289(4)	0	0.8	0.5	Bi(2)–O(3)	2.54(6)	x2
O(3)	*8f*	0.233(1)	0.266(6)	0.296(1)	0.8	1	Bi(2)–O(1)	2.31(6)	x1
							WMn–O(1)	1.74(3)	x2
			Space group *Cm2m*				WMn–O(2)	1.82(7)	x2
			a = 5.467(4) Å, b = 5.466(7) Å, c = 14.159(3) Å				WMn–O(2)	2.09(9)	x2
			R_p = 12.9%, R_{wp} = 16.1%, R_B = 5.87%						

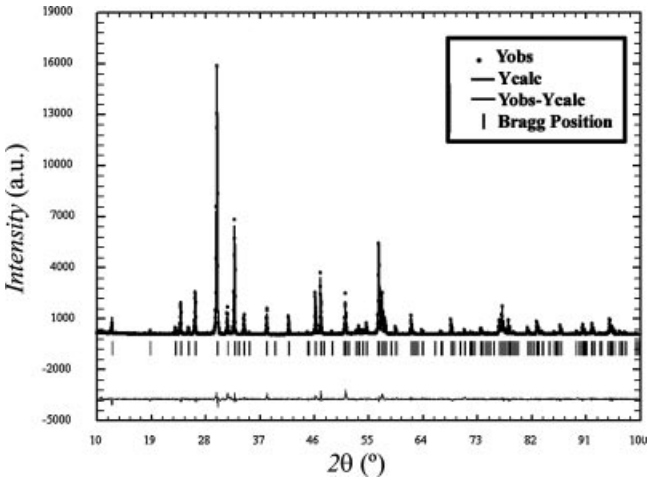

Figure 7. Experimental (circles), calculated and difference (solid lines) powder X-ray diffraction patterns of the $Bi_4Mn_{1/3}W_{2/3}O_8Cl$ phase. Vertical bars indicate the calculated Bragg angle positions.

is due to an asymmetric surrounding around the Bi_2O_2 layer; Bi(1) is close to the Cl sheet whereas Bi(2) is much closer to the $\{BO_6\}$ octahedral layer and can establish short contacts to the apex oxygen atoms O(1) (see Table 4), changing its coordination from 4 to 5, as can be seen in the structural model built for the new Sillén–Aurivillius intergrowth (Figure 8, a).

Within the distorted octahedra $(W/Mn)O_6$, the W/Mn–O(1) bonds are shorter than the W/Mn–O(2) bonds. This observation can be understood in terms of the Jahn–Teller effect originated by the Mn^{3+} cation replacing the W^{6+}. It is known that while the W^{6+} cation is spherical and symmetric, the Mn^{3+} cation causes a Jahn–Teller effect (compression or elongation). In this case, the presence of Mn^{3+} determined by the previous magnetic susceptibility measurements confirms the Jahn–Teller effect, giving rise to an average compression of the MnO_6 octahedra involving a decrease of the apical bonds. This phenomenon is described in more detail in ref.[18]

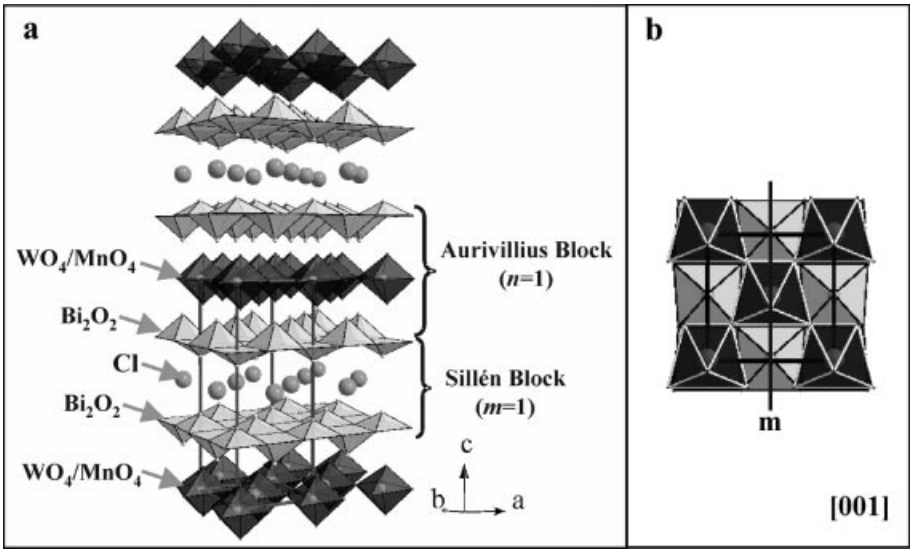

Figure 8. (a) Structure model of the Sillén–Aurivillius intergrowth $[Bi_2O_2][A_{n-1}B_nO_{3n+1}][Bi_2O_2][X_m]$ for n = 1 and m = 1. The stacking along c shows the Aurivillius block with the octahedral sheet (WO_4/MnO_4) sandwiched between the square pyramidal layers (Bi_2O_2) and the Sillén one with a chlorine (Cl) monolayer. The unit cell is marked by a continuous line. (b) Structural projection along [001] showing in dark grey the distorted octahedra of the perovskite layer.

These distorted polyhedra are shown in Figure 8 (b), where the structure of this new phase $Bi_4Mn_{1/3}W_{2/3}O_8Cl$ is projected along [001], presenting the lower space group *Cm*2*m* (instead of *P*4/*mmm*) demonstrated previously by microdiffraction observations.

Conclusions

A new phase with nominal composition $Bi_4Mn_{1/3}W_{2/3}O_8Cl$ is synthesised. The composition and homogeneity of the sample is determined by XEDS and EELS, whereas the oxidation state of Mn^{3+} is confirmed by magnetic susceptibility measurements.

The unit-cell symmetry and the space group are determined from microdiffraction and SAED experiments yielding an orthorhombic unit cell ($a \approx b$ = 5.4 Å and c = 14.1 Å) with space group *Cm*2*m*. A direct structural model is retrieved from a focal series of HREM images along the [1–10] zone axis. From the phase of the reconstructed exit-wave the projected coordinates can be directly determined. This model is used as input for a Rietveld refinement of the powder X-ray diffraction data.

Experimental Section

Preparation of the Samples: A polycrystalline sample with nominal composition $Bi_4Mn_{1/3}W_{2/3}O_8Cl$ was prepared by heating stoichiometric amounts of the oxides Bi_2O_3 (4N), WO_3 (4N), Mn_2O_3 (4N) and BiOCl (4N) at 993 K for a week in an evacuated (P = 10^{-4} Torr) sealed silica tube. The sample was then slowly cooled to room temperature for 24 h.

Characterisation Techniques: Samples for transmission electron microscopy (TEM) were prepared by ultrasonic dispersion of the crystals in *n*-butanol. Drops of this dispersion were deposited on a holey carbon-coated copper grid. A JEOL 2000FX equipped with a LINK ISIS 300 analyser was used for XEDS analysis, microdiffraction and SAED. The EEL spectra were acquired using a Philips CM200 FEG TEM equipped with a Gatan Image Filter (GIF) 200. High-resolution electron microscopy (HREM) was performed using a JEOL 3000F TEM and a Philips CM30 FEG TEM, yielding an information limit of 1.1 Å. The exit wave was reconstructed from the focal series using TrueImage software.[21] HREM image simulations were performed with NCEMSS software.[22]

X-ray powder diffraction patterns were recorded with a Siemens D-501 (Cu-$K_{\alpha 1}$ radiation λ = 1.5406 Å) over the angular range 10–100°, with a step scan of 0.04°. Rietveld full-profile refinement was done with the FULLPROF program.[23] A pseudo-Voigt function was chosen to generate the line shape of the diffraction peaks. In the final runs, the following parameters were refined: scale factor, background point to point, unit-cell parameters, asymmetry parameters, positional coordinates and isotropic thermal parameters. Further details of the crystal-structure investigation may be obtained from the Fachinformationszentrum Karlsruhe, 76344 Eggenstein-Leopoldshafen, Germany, on quoting the depository number CSD-416293.

Magnetic susceptibility measurements were performed on polycrystalline samples between 2 and 300 K, using a Quantum Design SQUID MPMS-X.

Acknowledgments

This work was supported by the CYCIT project MAT-2000-0753-C02-01. D. Á.-B. is grateful to MECD for a predoctoral grant and S. B. is grateful to the Fund for Scientific Research – Flanders.

[1] K. A. Yee, T. A. Albright, D. Jung, M. H. Whangbo, *Angew. Chem. Int. Ed. Engl.* **1989**, *28*, 750–751.
[2] R. L. Withers, J. G. Thompson, L. R. Wallenberg, J. D. Fitzgerald, J. S. Anderson, B. G. Hyde, *J. Phys. C: Solid State Phys.* **1988**, *21*, 6067–6083.
[3] A. F. Wells, *Structural Inorganic Chemistry*, 5th ed., Clarendon Press, Oxford, UK, **1984**.
[4] B. Aurivillius, *Arkiv. Kemi* **1949**, *1*, 463–480.
[5] J. F. Scott, *Ferroelectrics Rev.* **1998**, *1*, 1–130.
[6] J. F. Scott, *Phys. World* **1995**, *8*, 46.
[7] A. J. C. Wilson, *Structure Reports*, Oosthoek, Utrecht, **1947**, vol. 11.
[8] B. Aurivillius, *Chem. Scr.* **1984**, *23*, 143–156.
[9] J. F. Ackerman, *J. Solid State Chem.* **1986**, *62*, 92–104.
[10] A. M. Kusainova, S. Y. Stefanovich, V. A. Dolgikh, A. V. Mosunov, C. H. Hervoches, P. Lightfoot, *J. Mater. Chem.* **2001**, *11*, 1141–1145.
[11] C. N. Rao, B. Raveau, *Colossal Magnetoresistance, Charge Ordering and Related Properties of Manganese Oxides*, World Scientific, Singapore, **1998**.
[12] A. P. Ramirez, *J. Phys.: Condens. Matter* **1997**, *9*, 8171–8199.
[13] L. Smart, E. Moore, *Solid State Chemistry: An Introduction*, Chapman & Hall, London, **1992**, p. 240.
[14] J. P. Morniroli, J. W. Steeds, *Ultramicroscopy* **1992**, *45*, 219–239.
[15] T. Hahn, *International Tables for Crystallography*, vol. A, D. Reidel, Dordrecht, Holland, **1983**.
[16] D. Ávila-Brande, A. Gómez-Herrero, A. R. Landa-Cánovas, L. C. Otero-Díaz, *Solid State Sci.* **2005**, *7*, 486–496.
[17] D. Van Dyck, H. Lichte, K. D. Van der Mast, *Ultramicroscopy* **1996**, *64*, 1–15.
[18] S. Bals, S. Van Aert, G. Van Tendeloo, D. Ávila-Brande, *Phys. Rev. Lett.* **2006**, in press.
[19] W. J. Yu, Y. I. Kim, D. H. Ha, J. H. Lee, Y. K. Park, S. Seong, N. H. Hur, *Solid State Commun.* **1999**, *111*, 705–709.
[20] L. Y. Yang, L. Qiu, W. T. A. Harrison, R. Christoffersen, A. J. Jacobson, *J. Mater. Chem.* **1997**, *7*, 243–248.
[21] *TrueImage: Focal-series reconstruction package*,Version 1.0.2, FEI company, **2003**..
[22] *NCEMSS*, X-Window Version 1.8, R. Kilaar, December **2000**.
[23] Fullprof.2k, Version 1.9c, LLB, J. Rodriguez Carvajal, May **2001**.

Received: November 16, 2005
Published Online: March 13, 2006

